Nanoscale Advances

ROYAL SOCIETY OF CHEMISTRY

PAPER

View Article Online
View Journal | View Issue

Check for updates

Cite this: *Nanoscale Adv.*, 2020, **2**, 1269

Influence of Ga_2O_3, $CuGa_2O_4$ and Cu_4O_3 phases on the sodium-ion storage behaviour of CuO and its gallium composites

Rekha Pilliadugula,[a] Chandrasekaran Nithya[b] and N. Gopala Krishnan*[a]

Received 10th December 2019
Accepted 13th February 2020

DOI: 10.1039/c9na00773c

rsc.li/nanoscale-advances

CuO and its gallium composites with various compositions are successfully fabricated by using a hydrothermal technique followed by calcination at 900 °C. The added Ga precursors formed oxides in the composites, such as Ga_2O_3, $CuGa_2O_4$ and Cu_4O_3, as confirmed through the X-ray diffraction patterns as well as the HRTEM and SAED patterns. Further HRTEM analysis also confirmed that Cu_4O_3 and $CuGa_2O_4$ phases reside on the surface of CuO in the composites with a CuO : Ga ratio of 90 : 10. The contents of various oxide phases varied when we increased the amount of Ga in the CuO composites. Changing the ratios of CuO and Ga precursors in the composites is quite effective in tailoring the sodium-ion storage behaviour of CuO. The resultant CuO/Ga composites exhibit remarkable electrochemical performance for sodium-ion batteries in terms of capacity, rate capability and cycling performance. The composite containing 90% CuO and 10% Cu/Ga oxides delivers the highest charge capacity of 661 mA h g^{-1} at a current density of 0.07 A g^{-1} with a capacity retention of 73.1% even after 500 cycles. The structure and morphology of the composite (90% CuO and 10% Cu/Ga oxides) was successfully retained after 500 cycles, which was confirmed through *ex situ* XRD, SEM and HRTEM analyses. The composite also exhibited remarkable rate capability in which it delivered 96 mA h g^{-1} even at a high current density of 6.6 A g^{-1}. The enhanced electrochemical performances of CuO and its gallium composites are attributed to the presence of Cu_4O_3 and $CuGa_2O_4$ phases. The Cu_4O_3 phase is actively involved in the redox reaction and the $CuGa_2O_4$ phase stabilizes the CuO phase and buffers the volume expansion of CuO during cycling. The present approach eplores great opportunities for improving the electrochemical performance of oxide based anode materials for sodium-ion batteries.

1. Introduction

To avoid sporadic power generation, it is highly necessary to develop an efficient system with a controllable and constant electrical energy supply in order to meet the demands of the spectrum of energy needs which vary depending on the scale of consumption (from large to house-hold).[1,2] The electrical grid, owing to its inefficient storage, requires replacement with effective electrical energy storage technology.[3] Electrical energy storage (EES) establishes a balance between peak generation and peak demand. A timely response to demand can be successfully achieved by electro-chemical energy storage systems (ECESSs), which makes them commercially eminent sources for EES. ECESSs based on batteries have been proposed to be a potential alternative EES technology to the grid and its associated energy storage due to their standout features like cost benefits and sustainable energy supply with eminent cycling efficiency and cycle life.[1,4,5] Moreover, batteries can feasibly be used in a variety of high-end applications combined with different working conditions, ranging from large to local energy storage and supply, on account of their compactness in size.[1,2]

According to the increasing needs of today's market, there have been many types of batteries that work based on ionic electrochemistry. A few of these types attracted commercial attention due to their salient features meant to meet current market demands. Among them, rechargeable lithium ion batteries (LIBs) have acquired commerciality owing to their high values of theoretical capacity.[2,6–9] Though LIBs are famous in EES, they have their own challenges due to lithium being a rare and irregularly abundant element on earth.[2,10] In this context, sodium ion batteries (NIBs) came into the picture with huge and worldwide abundance and higher electrochemical potential (0.3 V greater than Li, *i.e.*, −2.71 V) than LIBs, which made them relatively cost-effective, and they have the same working features as LIBs.[2,11–15] Apart from their advantages, the applicability of NIBs for EES faces a challenge due to the limited

---

[a] Department of Physics, National Institute of Technology, Tiruchirappall-620015, Tamil Nadu, India. E-mail: ngk@nitt.edu; Tel: +431-2503607

[b] Department of Chemistry, PSGR Krishnammal College for Women, Peelamedu, Coimbatore-641004, Tamil Nadu, India

theoretical capacities of various materials due to the greater ionic size of Na^+ over Li^+.[11,13,15–18] The major types of materials used as anode materials for NIB applications so far are: carbonaceous materials, metal oxides, metal sulphides, organic and alloy materials, transition metal selenides and transition metal oxides.[19,20] Metal oxides are potential candidates for this application due to their good redox potentials, sound energy densities and effective safety features.[15] The limited conductivity, slow rate of Na^+ kinetics in metal oxide structures and volumetric variations and collapsibility of the structures of metal oxide materials result in low coulombic efficiency, below par rate performance and impairment of cyclability, respectively, limiting their potential as anode materials in NIBs.[15] These challenges imposed by metal oxide anode materials need to be dealt with to improve the hindered potential of these materials. The major concerns related to metal oxide based anode materials for NIBs include improvement of capacity, rate capability and cyclic stability, which highly depend on structural and chemical evolution of these materials upon electrochemical redox reactions that take place during sodiation/desodiation processes.

Among transition metal oxides, copper oxide (CuO) gained particular attention with a high theoretical capacity of 674 mA h g^{-1}.[15,21–25] Enhanced attention was paid to CuO as an anode material due to its global abundance, cost-effectiveness, high chemical stability and almost non-toxic nature. Much research was carried out on CuO based anode materials for LIBs.[21,25] Inauspiciously, as mentioned earlier, there are also concerns about the cyclability of CuO due to significant volume variations and structure collapse during electrochemical conversion reactions.[15,21–25] The issue of low conductivity is one more concern to be dealt with for NIBs. Several investigations have been dedicated to overcoming these problems. The preparation of composites with conductive and tough architectures is one way to overcome concerns related to low conductivity and structure collapse.[26,27] Synthesis of porous materials to facilitate volume changes in the active anode material, forming 1D nanostructures to limit or reduce the ionic diffusion path lengths, and preparation of composites with carbonaceous materials to improve the electronic/ionic conductivity are some of the strategies developed to enhance the performance of CuO as an anode material. Wang *et al.* reported porous CuO nanowires as an anode material for rechargeable NIBs.[28] Liu *et al.* used nanorod arrays grown on Cu substrate as an anode material for NIBs.[29] Yuan *et al.* reported the performance of nanosheets as an anode material for NIBs.[30] Composites of CuO with carbonaceous materials exhibit improved reversibility.[26,27,31] CuO quantum dots encapsulated in carbon nanofibers showed high reversible capacity and were successfully reported by Wang *et al.* as a binder free anode material for NIBs.[32] Li *et al.* reported that CuO/rGO composites achieved 470 mA h g^{-1} at a current density of 100 mA g^{-1} and 350 mA h g^{-1} at 2000 mA g^{-1}.[27] Sanghun *et al.* proposed a novel single step synthesis method for copper oxide/graphite composite materials that were used as anode materials for rechargeable batteries, in which the interlayer distance of graphite was elevated to a higher value, resulting in high capacity and long-term cycling stability.[33] Another major problem associated with metal oxide anode materials is volume expansion and structure collapse, which eventually worsens the cycling stability and capacity. Huggins and Besenhard experimented on the usage of alloyed metal oxides for the first time and succeeded in making them better anode materials for energy storage devices.[34–36] Introduction of an electrochemically inactive matrix into the anode material improves the cycling stability as the inactive matrix supports the active material by buffering volumetric changes during electrochemical reversible reactions.[37] The presence of an inactive matrix enormously reduces the obtainable capacity of the material. Thus, there is huge demand to study and understand the conversion reactions that take place in the presence of an inactive matrix in order to estimate the optimized amount for having a benign effect on the performance of the cell. In this work we investigate the anodic performance of CuO loaded with Ga in different weight percentages for NIBs. Further, we analyzed the influence of Cu_4O_3, $CuGa_2O_4$ and Ga_2O_3 phases on the electrochemical performance of CuO for NIBs.

2. Experimental section

2.1 Synthesis of pristine CuO and its gallium composites

A copper precursor solution was prepared by adding 2.815558 g of copper sulphate pentahydrate ($CuSO_4 \cdot 5\ H_2O$) (purchased from Alfa Aesar, 99.9% pure) to 120 mL of double distilled water under magnetic stirring. Once a homogeneous solution was obtained, 0.225 M concentrated NaOH solution was mixed into the copper sulphate solution at room temperature. After obtaining a homogeneous solution upon magnetic stirring, the final pH of the solution was found to be 5, and the solution mixture was transferred into a 200 mL autoclave which was then heat treated at 100 °C for 5 h in a muffle furnace. After cooling the solution down naturally to room temperature, the ensuing blue coloured precipitate was filtered and washed with double distilled water and ethanol several times. The obtained precipitate was then dispersed in double distilled water and dried in a hot air oven at 75 °C overnight. The obtained powder sample was then calcined at 900 °C for 5 h to get black coloured copper oxide (CuO) powders whose chemical phase was confirmed through XRD analysis. To prepare the gallium copper oxide composites, gallium nitrate hydrate ($Ga(NO_3)_3 \cdot xH_2O$) (purchased from Alfa Aesar, 99.9% pure) was added at 5, 10, 15 and 20 wt%, whereas $CuSO_4 \cdot 5H_2O$ was added at 95, 90, 85 and 80 wt%. Both the gallium and copper precursors were added in the appropriate weight percentages to double distilled water, and 0.225 M NaOH solution was added to this homogeneous precursor solution in all cases. The same synthesis procedure was followed for all weight ratios as described for pristine CuO synthesis. Post-calcination, the powder samples with Ga loaded at 0, 5, 10, 15 and 20 wt% were named as CGO-0, CGO-5, CGO-10, CGO-15 and CGO-20, respectively, and these codes are used to refer to them throughout this paper. Scheme 1 shows a schematic illustration containing the synthesis and cell design.

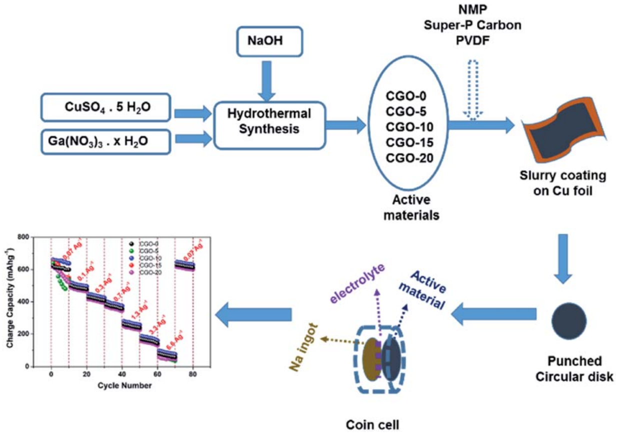

Scheme 1 Schematic illustration of synthesis and cell design.

2.2 Physical characterization

All the synthesized materials were structurally characterized using a Rigaku Ultima-III X-ray diffractometer with Cu-K$_\alpha$ radiation ($\lambda = 1.5406$ Å). Morphological and elemental analyses were carried out using a Carl Zeiss-Sigma Scanning Electron Microscope with EDAX provision. HRTEM (high resolution transmission electron microscope) images and SAED (selected area electron diffraction) patterns of CGO-10, before and after cycling, were obtained using a Jeol/JEM 2100 HRTEM. The composition and the oxidation states of different elements in CGO-10 were analyzed by X-ray photoelectron spectroscopy (XPS) with a scan range of 1200 eV. Surface area and pore size analyses of CGO-10 were carried out using N_2 adsorption–desorption curves obtained by using the Brunauer–Emmett–Teller method, and the data were obtained on a Micrometrics ASAP 2010 Physisorption & Porosimetry system. Pore size distributions were obtained by employing BJH analysis on the desorption branch.

2.3 Electrochemical characterization

The working electrode was prepared by using the traditional slurry coating method in which 80% synthesized active material was mixed with 10% super-P carbon and 10% PVDF binder. Here, super-P carbon acts as a conductive additive. *N*-methylpyrrolidone was used as a solvent to prepare the slurry homogeneously. The as-obtained homogeneous slurry was coated onto copper foil using an electrode coater and dried under ambient conditions. Circular discs of 18 mm diameter were punched out and dried under vacuum at 120 °C for 12 hours. 2032 type coin cells were finally assembled in an argon filled glove box in which the as-obtained disk was used as the working electrode and a sodium ingot was used as the reference electrode. The electrolyte was sodium perchlorate ($NaClO_4$) in 1 : 1 ethylene carbonate/diethyl carbonate (EC/DEC) (1 : 1 v/v), and Celgard 2400 was used as a separator. The galvanostatic charge/discharge studies were carried out on a programmable battery tester (NEWARE battery analyzer) at various current densities within the potential window between 0.01 and 3 V. The cyclic voltammetry (CV) and electrochemical impedance spectroscopy (EIS) studies were carried out on an electrochemical workstation (SP-150, Biologic SAS, France). The CV studies were carried out between the potential limits of 0.01 and 3 V at a scan rate of 0.1 mV s^{-1}. The EIS studies were carried out with an AC voltage signal of 5 mV and a frequency range between 100 kHz and 5 mHz.

3. Results and discussion

3.1 XRD analysis

Samples of pure copper oxide and composites of copper and gallium oxides containing 5, 10, 15 and 20 wt% of gallium precursor (*i.e.*, $Ga(NO_3)_3 \cdot xH_2O$), calculated with respect to copper precursor (*i.e.*, $CuSO_4 \cdot 5H_2O$) weight, were structurally

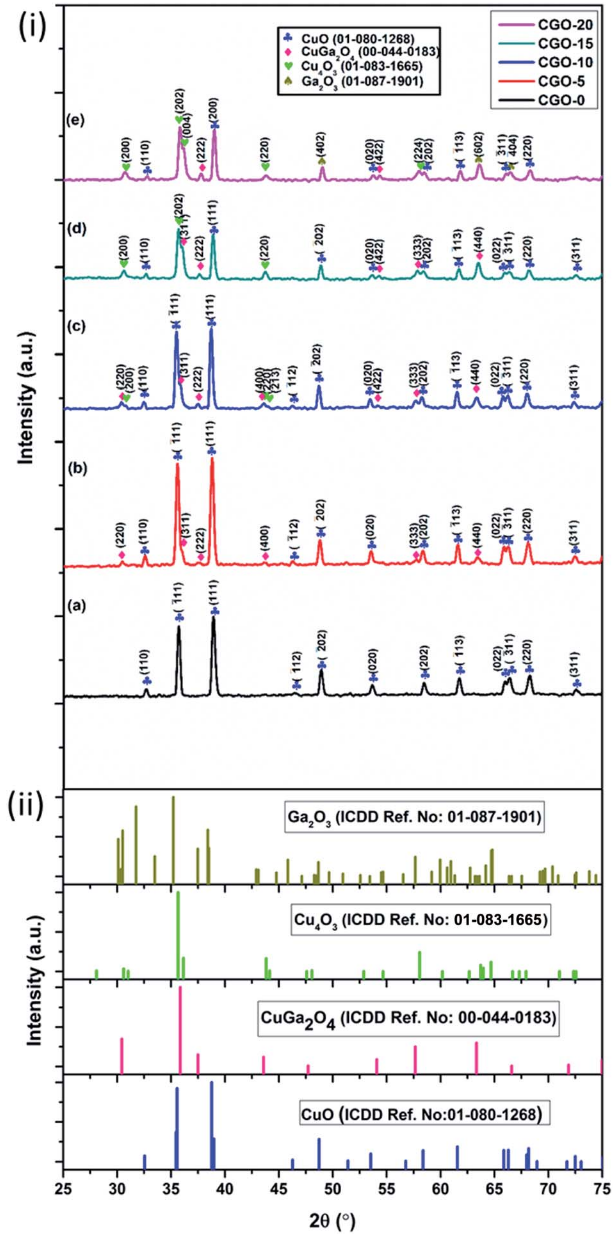

Fig. 1 (i) XRD patterns of (a) CGO-0, (b) CGO-5, (c) CGO-10, (d) CGO-15, and (e) CGO-20; (ii) reference XRD patterns of CuO, $CuGa_2O_4$, Cu_4O_3 and Ga_2O_3.

analysed by XRD. The obtained patterns of CGO-0, CGO-5, CGO-10, CGO-15 and CGO-20 are shown in Fig. 1. The phases of the synthesized samples matched well with the standards in the ICSD database. Through phase confirmation, it has been ascertained that there are four oxide phases of Cu and Ga found in the synthesized composites. They are CuO (copper oxide), copper gallium oxide ($CuGa_2O_4$), paramelaconite (Cu_4O_3) and gallium oxide (β-Ga_2O_3), which matched well with the ICSD standard patterns with reference numbers 01-080-1268, 00-044-0183, 01-083-1665 and 01-087-1901, and have monoclinic (space group: $C2/c$), cubic (space group: $Fd3m$), tetragonal (space group: $I4_1/amd$) and monoclinic (space group: $C2/m$) structures, respectively. CGO-0 showed diffraction peaks corresponding to CuO alone, whereas when the gallium precursor was introduced at 5 wt%, CGO-5 showed peaks for CuO and $CuGa_2O_4$. In addition to these two phases, CGO-10, CGO-15 and CGO-20 also

Table 1 Crystal systems, lattice parameters, crystallite sizes and micro strains of various phases corresponding to all samples

Sample code	Phase	Crystal system	Lattice parameters		Crystallite size (nm)	Micro strain ($\times10^{-3}$)
CGO-0	CuO	Monoclinic	a (Å)	4.7508 ± 0.0251	15.69	−2.14
			b (Å)	3.4328 ± 0.0284		
			c (Å)	5.1985 ± 0.208		
			Beta (°)	97.2681 ± 0.576		
			Unit cell volume V (Å)^3	84.254		
CGO-5	CuO	Monoclinic	a (Å)	4.7357 ± 0.2511	16.89	−1.84
			b (Å)	3.4181 ± 0.0379		
			c (Å)	5.1741 ± 0.2039		
			Beta (°)	98.08 ± 0.0578		
			Unit cell volume V (Å)^3	82.922		
	$CuGa_2O_4$	Cubic	a (Å)	8.3269 ± 0.0200	7.04	−4.67
			Unit cell volume V (Å)^3	577.369		
CGO-10	CuO	Monoclinic	a (Å)	4.6905 ± 0.0053	81.62	0.11
			b (Å)	3.4262 ± 0.0034		
			c (Å)	5.1398 ± 0.0204		
			Beta (°)	99.59 ± 0.18		
			Unit cell volume V (Å)^3	81.446		
	$CuGa_2O_4$	Cubic	a (Å)	8.3066 ± 0.0060	50.41	−0.15
			Unit cell volume V (Å)^3	573.143		
	Cu_4O_3	Tetragonal	a (Å)	5.8308 ± 0.0027	2.60	−15.63
			c (Å)	9.9541 ± 0.0063		
			Unit cell volume V (Å)^3	338.426		
			c/a	1.7072 ± 0.0011		
CGO-15	CuO	Monoclinic	a (Å)	4.6697 ± 0.0219	42.32	−0.12
			b (Å)	3.4166 ± 0.0043		
			c (Å)	5.1344 ± 0.0107		
			Beta (°)	99.56 ± 0.38		
			Unit cell volume V (Å)^3	80.777		
	$CuGa_2O_4$	Cubic	a (Å)	8.2680 ± 0.055	13.43	−2.56
			Unit cell volume V (Å)^3	565.208		
	Cu_4O_3	Tetragonal	a (Å)	5.8195 ± 0.002	18.04	−1.57
			c (Å)	9.9524 ± 0.0052		
			Unit cell volume V (Å)^3	336.25		
			c/a	1.7106 ± 0.0021		
CGO-20	CuO	Monoclinic	a (Å)	4.6919 ± 0.0102	40.93	−0.40
			b (Å)	3.4088 ± 0.0097		
			c (Å)	5.0601 ± 0.0384		
			Beta (°)	99.61 ± 0.20		
			Unit cell volume V (Å)^3	79.96		
	$CuGa_2O_4$	Cubic	a (Å)	8.2145 ± 0.0015	5.50	−7.23
			Unit cell volume V (Å)^3	559.16		
	Cu_4O_3	Tetragonal	a (Å)	5.8038 ± 0.0022	11.77	−2.81
			c (Å)	9.9497 ± 0.0058		
			Unit cell volume V (Å)^3	335.144		
			c/a	1.7143 ± 0.0010		
	Ga_2O_3	Monoclinic	a (Å)	5.8002 ± 0.0015	58.85	0.11
			b (Å)	3.26814 ± 0.0016		
			c (Å)	12.2508 ± 0.0010		
			Beta (°)	103.98 ± 0.18		
			Unit cell volume V (Å)^3	231.25		

showed peaks for the Cu_4O_3 phase, and CGO-20 exhibited peaks corresponding to Ga_2O_3 in addition to the prior mentioned oxide phases. The XRD patterns of all samples showed no traces of additional phases to the prior mentioned ones. The content of each phase was calculated as a percentage in terms of the ratio of the integral intensity of each phase over the sum of the integral intensities of all phases present in the sample, as reported in Table 1. The percentage of CuO phase was found to be 100%, 83.90%, 73.08%, 49.18% and 38.58% in CGO-0, CGO-5, CGO-10, CGO-15 and CGO-20, respectively. CGO-5 contained 16.10% $CuGa_2O_4$, whereas the $CuGa_2O_4$ content was found to be 22.90%, 27.25% and 6.59% in CGO-10, CGO-15 and CGO-20, respectively. The Cu_4O_3 content was estimated to be 4.02%, 23.57% and 39.25% in CGO-10, CGO-15 and CGO-20, respectively. The Ga_2O_3 phase has been found only in CGO-20, and its content has been found to be 15.59%. The presence of CuO decreased gradually with increasing Ga content from CGO-0 to CGO-20. Ga precipitated in the form of $CuGa_2O_4$ in CGO-5, CGO-10, CGO-15 and CGO-20, whereas in CGO-20, there is formation of Ga_2O_3 in addition to the $CuGa_2O_4$ phase, which shows that the abundance of Ga content in CGO-20 perturbed the equilibrium of $CuGa_2O_4$ phase formation which led to a favourable phase equilibrium for Ga_2O_3 and so lower probability for the formation of $CuGa_2O_4$. With an increase in Ga loading from 5 wt% to 10 wt%, Cu_4O_3 formation became more prominent. Cu_4O_3 started appearing in CGO-10 and the amount increased with Ga loading until CGO-20. As β-Ga_2O_3 is known to be a relatively electrochemically inactive phase,[38] CGO-20 is speculated to show poor electrochemical anodic performance among all the samples owing to its relatively greater content of Ga_2O_3. It has been proved that both CuO and Cu_4O_3 are electrochemically active materials, and thus the presence of both of these phases may enhance the storage capability of the prepared composites. Thus, the presence of the novel phase $CuGa_2O_4$ plays a vital role in controlling the anodic activity of the material. It is expected that the $CuGa_2O_4$ phase is responsible for enhancing the anode material stability by means of buffering the structural collapse of the material that happens during electrochemical cycling. Based on this assumption, it is expected that the sodium-ion storage capability of CGO-5, CGO-10 and CGO-15 may be better than that of CGO-0 and CGO-20, owing to the $CuGa_2O_4$ content in them. Further, Cu_4O_3 was investigated as an anode material for LIBs and was shown to exhibit superior rate performance and lower polarization owing to its lower impedance than CuO.[39] Thus, the collective and optimized proportional presence of the CuO, $CuGa_2O_4$ and Cu_4O_3 phases in the composites is expected to affect the electrochemical performance of the composites. The contribution of instrumental error to the broadening of the peaks is corrected by following eqn (1), where the full width at half maximum (FWHM) of the XRD peak profile of a Si standard is used for calibration purposes. In eqn (1),[40,41] L_{observed} denotes the FWHM of the obtained XRD pattern, $L_{\text{instrument}}$ is the FWHM of the standard reference peak profile, and L_{hkl} is the FWHM of the peak corresponding to the (hkl) crystalline plane after instrumental correction. The crystallite size and micro strain of each phase in each sample are found by following the Williamson–Hall (W–H) method (Fig. 2) in which line broadening in XRD is assumed to be the result of a cumulative effect of finite crystallite size and micro strain. Thus, in this analysis these two effects on peak broadening are de-convoluted and the final equation is given in eqn (2), where L_{hkl} represents the

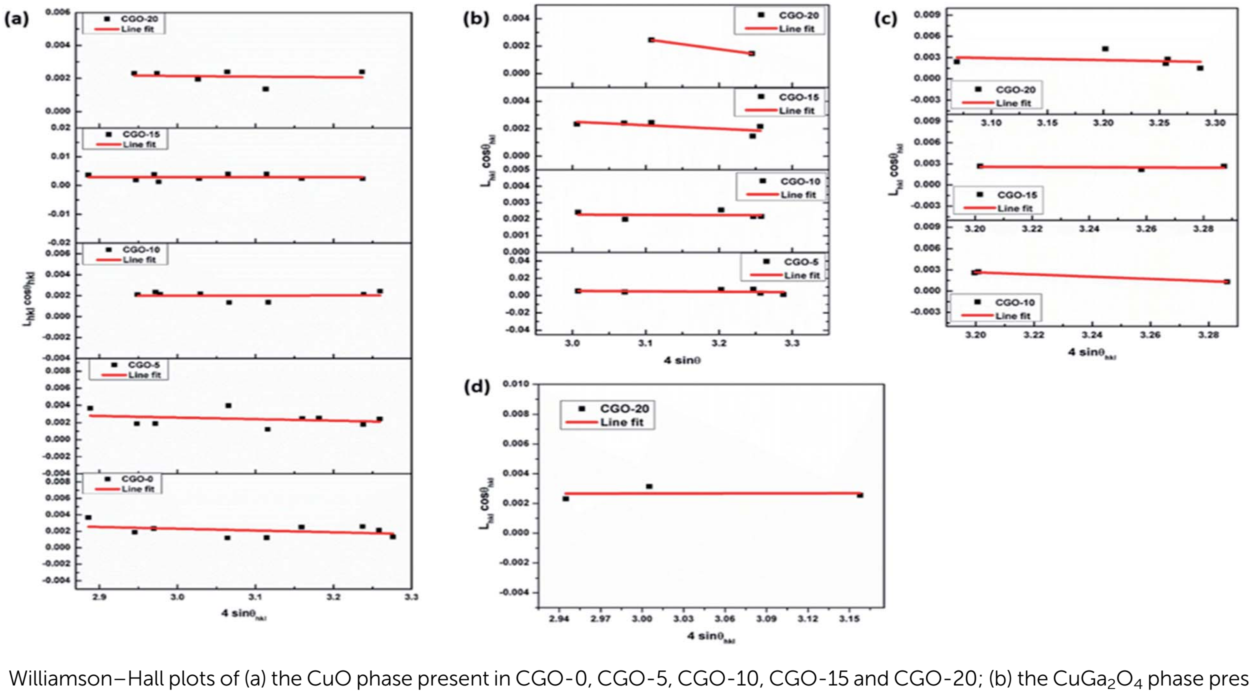

Fig. 2 Williamson–Hall plots of (a) the CuO phase present in CGO-0, CGO-5, CGO-10, CGO-15 and CGO-20; (b) the $CuGa_2O_4$ phase present in CGO-5, CGO-10, CGO-15 and CGO-20; (c) the Cu_4O_3 phase present in CGO-10, CGO-15 and CGO-20; (d) the Ga_2O_3 phase present in CGO-20.

FWHM of the (*hkl*) plane, θ_{hkl} is the Bragg diffraction angle corresponding to the (*hkl*) peak orientation, k denotes the shape factor, λ is the wavelength of the X-rays, ε is the strain and D denotes the crystallite size.[40,42–44] The W–H analytical method is considered to be an improved technique relative to Scherrer's method of analysis, as the strain contribution to peak broadening is neglected in Scherrer's equation.[40–44] The corresponding equation for the Scherrer method is given in eqn (3). In eqn (3), all variables have their usual meaning as described earlier. The crystallite sizes and micro strain values of the various chemical phases that are present in all samples under investigation are tabulated and shown in Table 1. Negative values of micro strain represent compressive strain whereas positive values indicate tensile strain.

$$L_{hkl} = \{(L_{\text{observed}}{}^2 - L_{\text{instrument}}{}^2)\}^{1/2} \tag{1}$$

$$L_{hkl}\cos\theta_{hkl} = \frac{k\lambda}{D} + 4\varepsilon\sin\theta_{hkl} \tag{2}$$

$$D = \frac{k\lambda}{L_{hkl}\cos\theta_{hkl}} \tag{3}$$

The lattice parameters of the unit cells corresponding to different phases were obtained by refining and fitting the XRD peaks of the corresponding phases, and the obtained values are shown in Table 1. It can be found from Table 1 that the CuO phase in CGO-0 showed a crystallite size of 15.69 nm, which is its lowest size among all the other samples and is accompanied by a compressive micro strain of 2.14×10^{-3}. The CuO phase showed crystallite sizes of 16.89, 81.62, 42.32 and 40.93 nm in CGO-5, CGO-10, CGO-15 and CGO-20, respectively. The crystallite sizes of $CuGa_2O_4$ in CGO-5, CGO-10, CGO-15 and CGO-20 are found to be 7.04, 50.41, 13.43 and 5.50 nm, respectively. The crystallite sizes of Cu_4O_3 are found to be 2.60, 18.04 and 11.77 nm in CGO-10, CGO-15 and CGO-20, respectively. Ga_2O_3, which existed only in CGO-20, was found to exhibit a crystallite size of 58.85 nm.

Naing *et al.*[45] and Liao *et al.*[46] showed that grain size enormously affects the electrochemical behavior of metal alloys. It has been proved that the coarser the crystallite, the better the rate performance, owing to larger grain boundary areas that allow diffusion of electrolyte ions through them, and finer crystallites in anode materials increase the cycle life, as they resist flow of electrolyte ions due to their narrower grain boundaries.[47] As mentioned earlier, CuO and Cu_4O_3 are electrochemically active materials, whereas the presence of Ga either in the form of a ternary oxide, $CuGa_2O_4$, or as a binary oxide, Ga_2O_3, worsens the electrochemical performance due to the redox inactive behavior of Ga. However, the presence of Ga with Cu, *i.e.* $CuGa_2O_4$, in the anode material may increase the cycle life by providing a buffering effect against structural collapse or volume expansions that take place in the active matrix during charge/discharge cycles. Moreover, Cu_4O_3 has been proved to exhibit superior rate performance and capacity retention over CuO and Cu_2O.[39] Thus, considering the above factors and the crystallite sizes obtained from XRD, it can be assumed that the large crystallite size of CuO in CGO-10 can lead to an improvement in rate performance, but may reduce the cycle life due to the formation of a greater quantity of residual phases. But, the presence of an inactive phase, *i.e.* $CuGa_2O_4$, with relatively larger crystallite size, and the presence of Cu_4O_3 with relatively finer crystallite size may increase the cycle life of the CGO-10 anode material among all the samples. Although CGO-10 is expected to show superior rate performance and cycle stability, CGO-5, CGO-10 and CGO-15 are also expected to show enhanced anodic performance compared to CGO-0. CGO-20, owing to the presence of inactive Ga_2O_3, may exhibit relatively lower electrochemical performance.

3.2 Morphological studies

Morphological observations are carried out through SEM micrographs as shown in Fig. 3. It has been observed that CGO-0 showed a beach stone-like morphology with irregular particle shapes. It is clear from Fig. 3 that introduction of gallium into the system promoted the precipitation of Ga phases on top of the CuO particles observed in Fig. 3a. This accumulation of secondary phases is clearly visible in the figure as tiny particles covering the CuO particles, and the coverage of the beach stone-like particles by powder-like particles increased from CGO-5 to CGO-20. In CGO-15 and CGO-20, the Ga phases became dominant and covered almost all of the CuO particles, and the CuO particles became almost invisible under microscopic scanning. The aspect ratios of the CuO particles in all samples are calculated as the ratio between the length of the longest dimension

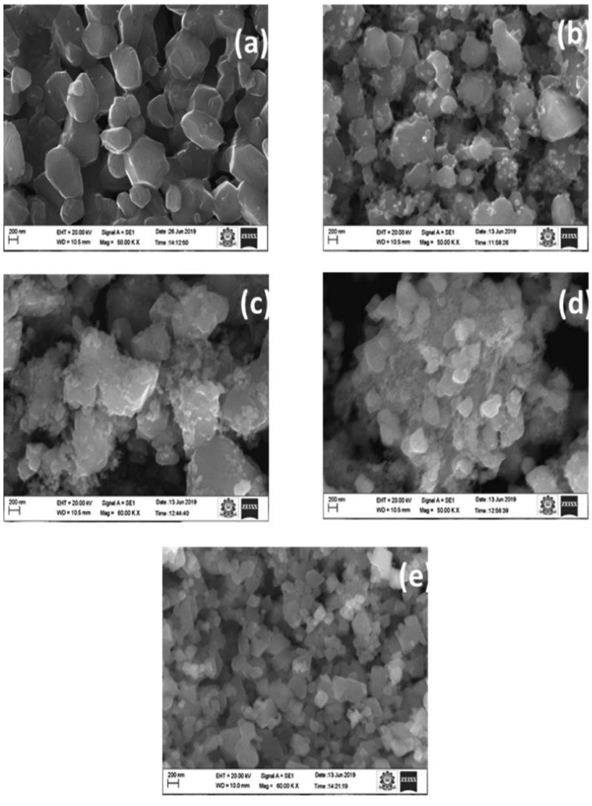

Fig. 3 SEM micrographs of (a) CGO-0; (b) CGO-5; (c) CGO-10; (d) CGO-15; and (e) CGO-20.

Table 2 Aspect ratios of CuO particles in all samples

Sample no.	Sample code	Aspect ratio
1	CGO-0	1.33
2	CGO-5	1.41
3	CGO-10	1.19
4	CGO-15	1.40
5	CGO-20	1.63

(along the length) of the particle to the diameter along the shortest dimension (along the breadth), as the particles are irregular in shape. The calculated average aspect ratios for all samples are given in Table 2. The aspect ratios of the particles varied irregularly from sample-to-sample and can be correlated with the formation of different binary and ternary oxides of Cu and Ga ($CuGa_2O_4$, Cu_4O_3) and the strain associated with their formation. It is evident that particles with lower dimensions can show relatively enhanced electrochemical performance, and thus it can be presumed that CGO-10, owing to its lower aspect ratio, may exhibit better rate performance.

Fig. 4 shows elemental analyses of the samples carried out through EDAX incorporated in the SEM. The atomic% and weight% of Cu, Ga and O are in accordance with the proportions of Cu and Ga precursors added. The Ga content increased with increasing Ga precursor wt%. Ga wt% in CGO-0, CGO-5, CGO-10, CGO-15 and CGO-20 are found to be 0 wt%, 7.2 wt%, 15.2 wt%, 22.7 wt% and 31.9 wt%, respectively. It can be said from these results that Ga incorporation into the base material was successfully carried out, and the deviation of these values from the added wt% of Ga is owing to the fact that the added wt% is based on the amounts of precursor salts used, not on the actual Ga content.

TEM micrographs of CGO-10 are shown in Fig. 5. These micrographs are consistent with those from SEM analysis. Fig. 5a clearly depicts small particles of Cu_4O_3 and $CuGa_2O_4$ on top of bigger particles of CuO. Fig. 5b is a magnified portion of the smaller particle aggregates, and their particle sizes varied in the range of 30–85 nm. An HRTEM image and the SAED pattern of CGO-10 are shown in Fig. 5c and d, respectively. Lattice fringes are clearly observed in CGO-10, in which the (220) diffraction planes corresponding to Cu_4O_3 and $CuGa_2O_4$ have *d*-spacings of 0.206 and 0.293 nm, respectively. Well defined bright spots formed into rings are observed in the SAED pattern, which shows that these samples are polycrystalline and the grains are monocrystalline. In the SAED pattern of CGO-10, the spots designated as a, b and c correspond to the CuO, $CuGa_2O_4$ and Cu_4O_3 phases and were assigned to the $(\bar{1}12)$, (220) and (200) planes with *d*-spacings of 0.196, 0.293 and 0.290 nm, respectively. All the *d*-spacing values found from the SAED pattern of CGO-10 are in good agreement with those found from the corresponding XRD pattern.

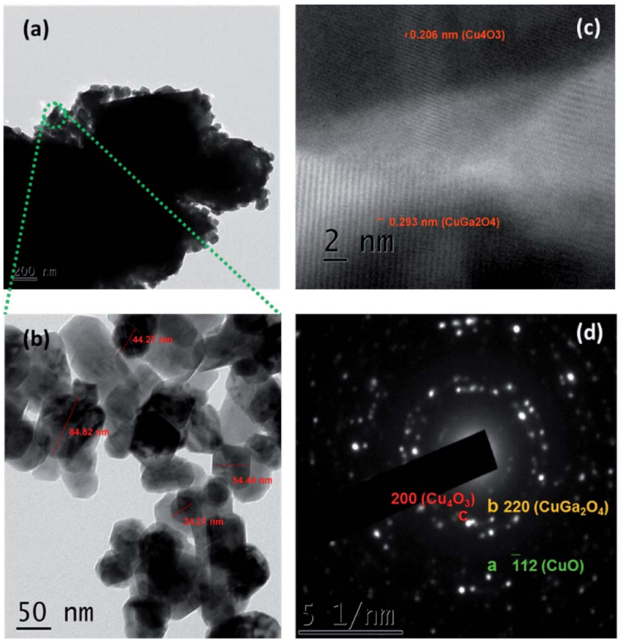

Fig. 5 TEM micrographs of CGO-10 at different magnifications: (a) 200 nm; (b) 50 nm; (c) HRTEM image and (d) SAED pattern of CGO-10.

3.3 BET analysis

The surface area of CGO-10 was obtained from BET N_2 adsorption–desorption studies. The N_2 adsorption–desorption profiles of CGO-10 are shown in Fig. 6a, and the corresponding

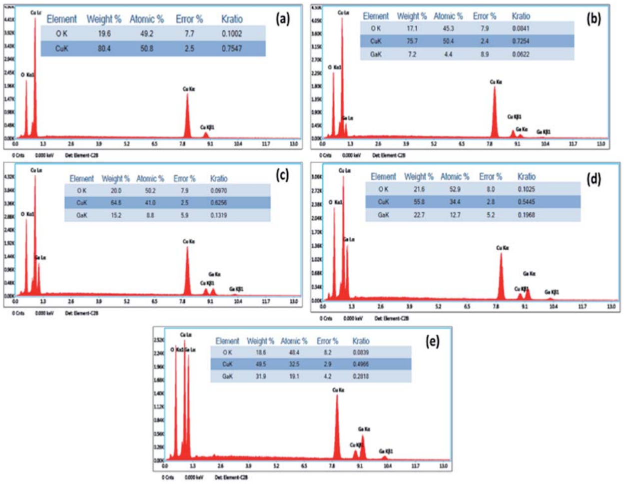

(a)

Element	Weight %	Atomic %	Error %	Kratio
O K	19.6	49.2	7.7	0.1002
CuK	80.4	50.8	2.5	0.7547

(b)

Element	Weight %	Atomic %	Error %	Kratio
O K	17.1	45.3	7.9	0.0841
CuK	75.7	50.4	2.4	0.7254
GaK	7.2	4.4	8.9	0.0622

(c)

Element	Weight %	Atomic %	Error %	Kratio
O K	20.0	50.2	7.9	0.0970
CuK	64.8	41.0	2.5	0.6256
GaK	15.2	8.8	5.9	0.1319

(d)

Element	Weight %	Atomic %	Error %	Kratio
O K	21.6	52.9	8.0	0.1025
CuK	55.8	34.4	2.8	0.5445
GaK	22.7	12.7	5.2	0.1968

(e)

Element	Weight %	Atomic %	Error %	Kratio
O K	18.6	48.4	8.2	0.0839
CuK	49.5	32.5	2.9	0.4966
GaK	31.9	19.1	4.2	0.2018

Fig. 4 EDAX plots with quantitative elemental analysis of (a) CGO-0, (b) CGO-5, (c) CGO-10, (d) CGO-15 and (e) CGO-20.

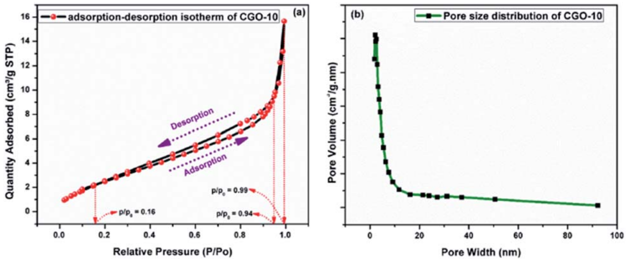

Fig. 6 (a) N_2 adsorption–desorption isotherm; (b) BJH pore size distribution of CGO-10.

pore size distribution is shown in Fig. 6b. As shown in Fig. 6a, CGO-10 showed a type-III isotherm for both the adsorption and desorption processes with an H3 type hysteresis loop according to the IUPAC classification.[46,47] H3 type hysteresis is a characteristic of meso sized pores, and the narrow loop appeared with a lower limit of $p/p_0 = 0.16$ up to $p/p_0 = 0.94$, exhibiting the dominance of mesoporosity in the sample. Also, a short and narrow loop appeared at high relative pressures between $p/p_0 = 0.94$ and $p/p_0 = 0.99$, which corresponds to a small amount of nearly macro sized pores. Fig. 6b shows the pore volume distribution as a function of pore width. The surface area of CGO-10 has been obtained from the N_2 adsorption–desorption profile by following the BET (Brunauer–Emmett–Teller) method, and the value was found to be 11.5171 $m^2\ g^{-1}$. The average pore diameter was obtained by employing the BJH (Barrett–Joyner–Halenda) analytical method on the desorption branch, and the pore diameter was found to be 5.2015 nm. The formation of pores on the particle surface may be due to the liberation of water and hydroxyl ions during calcination.[48,49]

3.4 XPS analysis

Investigations of the chemical bonding states of different elements in the CGO-10 sample are carried out through X-ray photoelectron spectroscopy (XPS). The XPS survey spectrum showed the presence of Cu, Ga and O in the sample (Fig. 7a). The XPS peaks of the elements mentioned above were deconvoluted using the Gaussian fitting function. The Cu-2p (Fig. 7b) scan exhibited four peaks among which two are satellite peaks and designated as S-1 and S-2 centred at 943.6 eV and 963.7 eV, respectively.[50] The Cu-2p scan also showed two strong photoelectron emissions de-convoluted at 935.4 eV and 955.3 eV, corresponding to the Cu-2$p_{3/2}$ and Cu-2$p_{1/2}$ electronic levels, respectively.[51,52] These are the characteristic peaks of

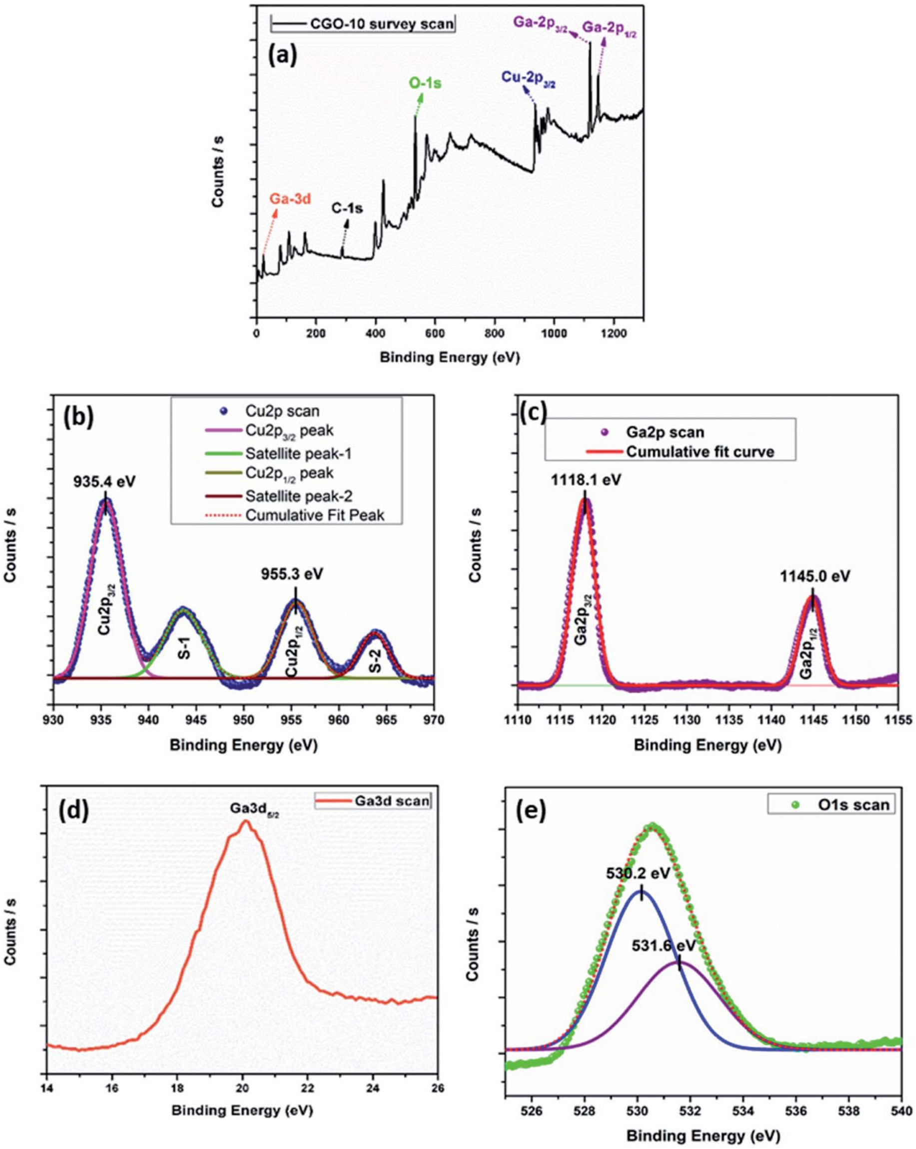

Fig. 7 XPS analysis of CGO-10: (a) survey spectrum, (b) Cu-2p, (c) Ga-2p, (d) Ga-3d and (e) O-1s.

Cu(II), and the Cu^{2+} oxidized charge state in $CuGa_2O_4$ exhibited a spin–orbit splitting energy separation of 19.9 eV which matched the previously reported values well.[51–54] The Ga-2p scan showed two peaks centred at 1118.18 eV and 1145.08 eV corresponding to Ga-$2p_{3/2}$ and Ga-$2p_{1/2}$, respectively, as shown in Fig. 7c[51], with an energy separation of 26.9 eV which matched the previously reported value well.[51,54,55] The Ga-3d scan shown in Fig. 7d exhibits a peak at around 20.08 eV corresponding to Ga-$3d_{5/2}$.[56–58] The O-1s XPS scan is shown in Fig. 7e and has two de-convoluted peaks, one centered at 530.2 eV that corresponds to metal–oxygen bonding,[52,59] and the other one at 531.6 eV, corresponding to surface absorbed O_2.[60] The slight shift of the O-1s peak towards higher binding energy than the reported values may be due to an interaction between the binary and ternary oxide phases present in the sample.[61] The observation of all the above described peaks in the sample gives evidence for the presence of CuO and $CuGa_2O_4$ in CGO-10.

3.5 Charge/discharge studies

In order to investigate the sodium storage behaviour of the CGO composites we examined the galvanostatic charge/discharge behaviour at 0.07 A g^{-1} between the potential limits 0.01 and 3 V. Fig. 8a presents the first charge/discharge curves of the CGO composites in which the composites delivered charge capacities of 624, 640, 661, 647 and 618 mA h g^{-1} for CGO-0, CGO-5, CGO-10, CGO-15 and CGO-20, respectively. The charge/discharge profiles of the composites vary from that of pristine CuO which indicates that Cu_4O_3 also participated in the electrochemical reaction of CuO for sodium-ion storage. It is interesting to note that though the charge/discharge profiles of CGO-10 and CGO-15 are identical, likewise the profiles of CGO-5 and CGO-20, all deviate from that of pristine CuO. The deviation is due to the formation of Cu_4O_3, $CuGa_2O_4$ and Ga_2O_3 phases in the composites. However, the content of the phases varied when the amount of Ga in the composites was increased from 5 to 20 wt%. Pristine CuO exhibited broad plateaus at around 0.82–0.5 V and 1.7–2.1 V in the discharge and charge curves, respectively. The broad plateau in the discharge curve represents the multiple reduction processes involved in solid–electrolyte interphase (SEI) formation on the electrode surface: intermediate $Cu^{II}_{1-x}Cu^{I}_{x}O_{1-x/2}$ phase formation, generation of the Cu_2O phase and the decomposition of Cu_2O to Cu and Na_2O. Similarly, the broad plateau in the charge profile indicates the reverse reaction of the discharge process. The composites exhibit three plateaus, *viz.* 0.3–0.14, 0.8–0.4 and 1.4–0.9 V in the discharge curve and three plateaus, *viz.* 0.4–0.78, 0.9–1.6 and 1.7–2.7 V in the charge curve. The three reduction plateaus of the composites are due to the intermediate phase formation of $Cu^{II}_{1-x}Cu^{I}_{x}O_{1-x/2}$ and SEI film formation, reduction of CuO to Cu_2O and further conversion of Cu_2O to Cu. The oxidation peaks correspond to the decomposition of the SEI film, the oxidation process of Cu to Cu_2O and further oxidation of Cu_2O to CuO. The three plateaus in the charge and discharge profiles are obtained at slightly different potentials for all the composites, which can be attributed to the variation in content of the Cu_4O_3, $CuGa_2O_4$ and Ga_2O_3 phases in different composites. The contents of the electrochemically active Cu_4O_3 and $CuGa_2O_4$ phases are higher in CGO-10 and CGO-15 but they are lower in CGO-5 and CGO-20. In CGO-5 and CGO-20, the electrochemically inactive β-Ga_2O_3 phase dominates the electrochemical process during cycling. The high capacities of CGO-10 and CGO-15 may be ascribed to the fact that the electrochemically active Cu_4O_3 phase[39,62] together with the $CuGa_2O_4$ phase enhances the capacity of the CuO phase. The Cu_4O_3 phase is also present in the case of CGO-5 and CGO-20, however, the content of $CuGa_2O_4$ is very low and there is more Ga_2O_3 in CGO-20 (β-Ga_2O_3 is known to be redox inactive[38]). Here, the $CuGa_2O_4$ phase may act as a matrix to enhance the capacity of CuO during electrochemical reactions.

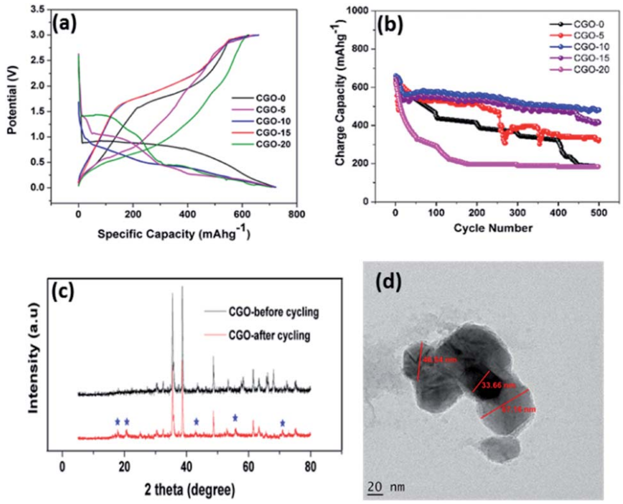

Fig. 8 (a) Charge/discharge behaviour of CuO/Ga_2O_3 at 0.07 A g^{-1}. (b) Cycling performance of CuO/Ga_2O_3 at 0.07 A g^{-1} over 500 cycles. (c) *Ex situ* XRD patterns of CGO-10. (d) TEM image of CGO-10 after cycling.

Fig. 8b depicts the cycling performance of the CGO composites at a current density of 0.07 A g^{-1} over 500 cycles. The first cycle charge capacities are 624, 640, 661, 647 and 618 mA h g^{-1} for CGO-0, CGO-5, CGO-10, CGO-15 and CGO-20, respectively, whereas at the 500th cycle the obtained charge capacities are 183, 319, 481, 415 and 183 mA h g^{-1}, respectively. The corresponding capacity retentions are 29.3, 49.8, 73.1, 64.1 and 29.6%, respectively. The obtained cycling performance clearly indicates that the cycling stability of CuO is greatly enhanced by the electrochemically active Cu_4O_3 phase together with the $CuGa_2O_4$ matrix. The inferior performance of CGO-0, CGO-5 and CGO-20 is attributed to large volume expansion[15] during the electrochemical reaction which resulted in loss of contact between the current collector and the electrode material. In order to investigate the stability of the electrode material after 500 cycles, we carried out *ex situ* XRD (Fig. 8c), TEM (Fig. 8d), *ex situ* SEM (Fig. 9a) and HRTEM (Fig. 9b and c) on the CGO-10 electrode. Interestingly, the structure and morphology of CGO-10 are well maintained even after 500 cycles. The *ex situ* XRD pattern of CGO-10 after cycling showed the characteristic peaks of CGO-10 with minor impurity peaks which may be due to the conductive carbon and binder used for the electrode

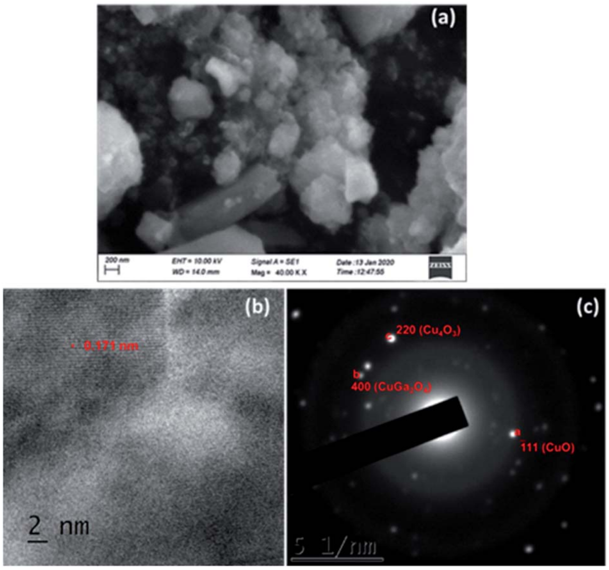

Fig. 9 (a) SEM image, (b) HRTEM image and (c) SAED pattern of CGO-10 after cycling.

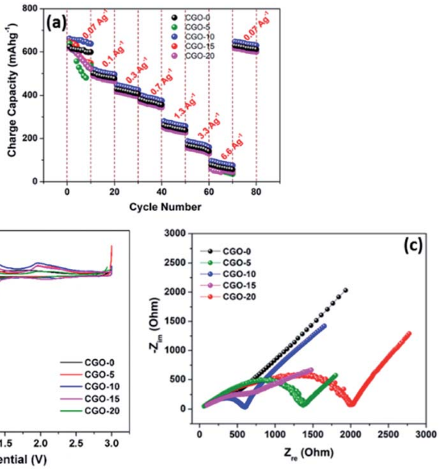

Fig. 10 (a) Rate capabilities of CuO/Ga$_2$O$_3$ composites at different current densities, (b) cyclic voltammograms of CuO/Ga$_2$O$_3$ at a scan rate of 0.1 mV s^{-1} and (c) Nyquist plots of CuO/Ga$_2$O$_3$ with different compositions.

coating. TEM and SEM images of CGO-10 after cycling are shown in Fig. 8d and 9a, respectively. There is no noticeable change in particle morphology and size even after prolonged cycling of the material. An HRTEM image of CGO-10 after cycling and the corresponding SAED pattern are shown in Fig. 9b and c, respectively. Lattice fringes are clearly observed in CGO-10 after cycling, and the (020) plane of CuO with a *d*-spacing of 0.171 nm is clearly observed in the HRTEM image of CGO-10 after cycling (from Fig. 9b). The well defined bright spots formed into rings in the diffraction pattern are attributed to the polycrystalline sample and the monocrystalline grains. The spots labelled a, b and c in the SAED pattern of CGO-10 after cycling are assigned to the ($\bar{1}$11), (400) and (220) diffraction planes corresponding to the CuO, CuGa$_2$O$_4$ and Cu$_4$O$_3$ phases with *d*-spacing values of 0.253, 0.207 and 0.206 nm, respectively. All the *d*-spacing values found from the SAED pattern of CGO-10 after cycling are in good agreement with those found from the corresponding XRD pattern. The above obtained results confirmed that the charge/discharge behaviour and cycling stability of the CuO material are greatly enhanced by the Cu$_4$O$_3$ phase and the CuGa$_2$O$_4$ matrix. The rate capability of the CuO/Ga$_2$O$_3$ composites was investigated between the potential limits of 0.01 and 3 V at different current densities, as shown in Fig. 10a. Compared to the other composites, the CGO-10 composite exhibits better rate capability, with charge capacities of 661, 519, 447, 401, 281, 187 and 96 mA h g^{-1} at current densities of 0.07, 0.1, 0.3, 0.7, 1.3, 3.3 and 6.6 A g^{-1}, respectively. It is interesting to note that the cell exhibited a charge capacity of 647 mA h g^{-1} when the cell is cycled back from high current density to low current density (0.07 A g^{-1}). The rate capability results confirmed that CGO-10 exhibits good rate performance and structural stability at high current densities. Aside from CGO-10, the other composites exhibited poor rate performance at high current densities. The obtained capacities and cycling stability are superior compared to previous literature.[27,63] In order to further understand the electrochemical reactions of the CGO composites, we carried out cyclic voltammetry studies (Fig. 10b) at a scan rate of 0.1 mV s^{-1} between the potential limits of 0.01 and 3 V. The cyclic voltammograms are quite consistent with the charge/discharge behaviour of the CGO composites. The cathodic peak was observed at 0.57 V and the anodic peak was observed at 1.95 V for the pristine CuO material. The broad cathodic peak corresponds to multiple reduction processes involved in the decomposition of the electrolyte solvents, *i.e.* EC and DEC, to form a SEI film on the electrode surface, the formation of an intermediate CuO phase, *i.e.* $Cu^{II}_{1-x}Cu^{I}_{x}O_{1-x/2}$, the generation of the Cu$_2$O phase and the decomposition of Cu$_2$O to Cu and Na$_2$O. During the charge process, a broad oxidation peak is observed at around 1.82 V, which corresponds to the oxidation process involved in the formation of the CuO phase from the Cu$_2$O phase. The obtained CV curve of CuO is quite consistent with the previously reported literature.[28] All the composites exhibited three reduction peaks, *viz.* 1.23, 0.7 and 0.28 V, during discharge and three oxidation peaks at 0.78, 1.28 and 1.98 V during charge. Like the charge/discharge profiles, the CV curves of CGO-10 and CGO-15 are quite similar, while those of CGO-5 and CGO-20 appear to be similar except for the redox peak intensities. The obtained CV profiles of the CGO composites are in accordance with the previously reported literature.[27] The highest capacities of the CGO composites are attributed to the combined redox reactions of CuO and Cu$_4$O$_3$, as we couldn't identify the peak signatures separately since Cu$_4$O$_3$ also forms a 2CuO + Cu$_2$O composite which itself exhibits several redox peaks according to L. Zhao *et al.*,[62] and the mechanism of storing lithium ions is still not clear. From the CV profiles we clearly confirmed that only the CuO and Cu$_4$O$_3$ phases are involved in the redox reactions, however the CuGa$_2$O$_4$ phase acts as an inactive matrix to stabilize the CuO phase during cycling.

In order to gain further insight into the charge/discharge profiles and CV curves of pristine CuO and CGO composites, we carried out EIS analysis and obtained Nyquist plots which

Table 3 EIS parameters of CGO composites

Sample no.	Sample	R_s (Ω)	R_{ct} (Ω)	C_{dl} (mF)
1	CGO-0	163	490	20
2	CGO-5	47	1323	48
3	CGO-10	101	516	72
4	CGO-15	83	772	61
5	CGO-20	324	1692	21

are shown in Fig. 10c. The EIS parameters are listed in Table 3. All Nyquist plots show one semicircle in the high frequency region and a line inclined at 45° in the low frequency region, which is called the Warburg region. This Warburg region is a signature of the Na^+ ion diffusion process occurring in the electrode material during cycling. Depressed semicircles are observed in the case of CGO-10 and CGO-15, whereas the other CGO composites exhibit semicircles with high R_{ct} (Table 3). This indicates that CGO-10 and CGO-15 exhibit lower impedance as compared to the other CGO composites. From the electrochemical studies we clearly confirmed that the enhanced electrochemical performances of the CGO composites are mainly attributed to the presence of Cu_4O_3 and $CuGa_2O_4$ phases, in which the Cu_4O_3 phase is actively involved in the redox reactions and the $CuGa_2O_4$ phase stabilizes the CuO phase by buffering the volume expansion of CuO during cycling.

4. Conclusion

In summary, we have fabricated CGO composites with different weight percentages of Ga through a simple hydrothermal method. The HRTEM images and SAED patterns confirmed that the particle size varies from 30 to 85 nm and also showed that the Cu_4O_3 and $CuGa_2O_4$ phases reside on the surface of the CuO phase. The composites exhibit significantly improved capacity and capacity retention as compared to the pure CuO phase at a current density of 0.07 A g^{-1}. The CGO-10 composite (CuO with 10 wt% Ga) exhibited the highest charge capacity of 481 mA h g^{-1} with capacity retention of 73.1% at a current density of 0.07 A g^{-1} over 500 cycles. The improved capacity and capacity retention of the composites are mainly attributed to the Cu_4O_3 phase as well as the $CuGa_2O_4$ phase, in which Cu_4O_3 effectively reduces the charge-transfer resistance and the $CuGa_2O_4$ phase buffers the volume expansion of the CuO particles during cycling. The obtained results demonstrate that the composites are considered as promising anode materials for sodium-ion batteries.

Conflicts of interest

There are no conflicts to declare.

Acknowledgements

One of the authors, Dr C. Nithya, wishes to thank the Department of Science and Technology (DST, India) for a Women Scientist Award (SR/WOS-A/CS-20/2017).

References

1 B. Dunn, H. Kamath and J. M. Tarascon, Electrical Energy Storage for the Grid: A Battery of Choices, *Science*, 2011, **334**, 928.

2 Y. You and A. Manthiram, Progress in High-Voltage Cathode Materials for Rechargeable Sodium-Ion Batteries, *Adv. Energy Mater.*, 2018, **8**, 1701785.

3 B. Guo, M. Niu, X. Lai and L. Chen, Application research on large-scale battery energy storage system under Global Energy Interconnection framework, *Global Energy Interconnection*, 2018, vol. 1, p. 79.

4 B. H. Rao, S. L. Arun and M. P. Selvan, Framework of Locality Electricity Trading System for Profitable Peer-to-Peer Power Transaction in Locality Electricity Market, *IET Smart Grid*, 2019, DOI: 10.049/iet-stg.2019.0131.

5 B. H. Rao, S. L. Arun and M. P. Selvan, An electric power trading framework for smart residential community in smart cities, *IET Smart Cities*, 2019, **1**, 40, DOI: 10.1049/iet-smc.2019.0055.

6 W. Zhang, Z. X. Chi, W. X. Mao, R. W. Lv, A. M. Cao and L. J. Wan, One-Nanometer Precision Control of Al_2O_3 Nanoshells through a Solution-Based Synthesis Route, *Angew. Chem., Int. Ed.*, 2014, **53**, 12776.

7 P. F. Wang, H. R. Yao, X. Y. Liu, J. N. Zhang, L. Gu, X. Q. Yu, Y. X. Yin and Y. G. Guo, Ti-substituted $NaNi_{0.5}Mn_{0.5-x}Ti_xO_2$ Cathodes with Reversible O3-P3 Phase Transition for High Performance Sodium-Ion Batteries, *Adv. Mater.*, 2017, **29**, 1700210.

8 L. Mu, S. Xu, Y. Li, Y. S. Hu, H. Li, L. Chen and X. Huang, Prototype Sodium-Ion Batteries Using an Air-Stable and Co/Ni-Free O3-Layered Metal Oxide Cathode, *Adv. Mater.*, 2015, **27**, 6928.

9 R. Y. Wang, C. D. Wessells, R. A. Huggins and Y. Cui, Highly Reversible Open Framework Nanoscale Electrodes for Divalent Ion Batteries, *Nano Lett.*, 2013, **13**, 5748.

10 C. Fang, Y. Huang, W. Zhang, J. Han, Z. Deng, Y. Cao and H. Yang, Routes to High Energy Cathodes of Sodium-Ion Batteries, *Adv. Energy Mater.*, 2016, **6**, 1501727.

11 J. Y. Hwang, S. T. Myung and Y. K. Sun, Sodium-ion batteries: present and future, *Chem. Soc. Rev.*, 2017, **46**, 3529.

12 H. Kim, H. Kim, Z. Ding, M. H. Lee, K. Lim, G. Yoon and K. Kang, Recent Progress in Electrode Materials for Sodium-Ion Batteries, *Adv. Energy Mater.*, 2016, **6**, 1600943.

13 D. Kundu, E. Talaie, V. Duffort and L. F. Nazar, The Emerging Chemistry of Sodium Ion Batteries for Electrochemical Energy Storage, *Angew. Chem., Int. Ed.*, 2015, **54**, 3431.

14 Y. Zhao, L. P. Wang, M. T. Sougrati, Z. Feng, Y. Leconte, A. Fisher, M. Srinivasan and Z. Xu, A Review on Design Strategies for Carbon Based Metal Oxides and Sulfides Nanocomposites for High Performance Li and Na Ion Battery Anodes, *Adv. Energy Mater.*, 2017, **7**, 1601424.

15 L. Wang, Z. Wei, M. Mao, H. Wang, Y. Li and J. Ma, Metal oxide/graphene composite anode materials for sodium-ion batteries, *Energy Storage Materials*, 2019, **16**, 434.

16 S. W. Kim, D. H. Seo, X. Ma, G. Ceder and K. Kang, Electrode Materials for Rechargeable Sodium-Ion Batteries: Potential Alternatives to Current Lithium-Ion Batteries, *Adv. Energy Mater.*, 2012, **2**, 710.

17 H. Pan, Y. S. Hu and L. Chen, Room-temperature stationary sodium-ion batteries for large-scale electric energy storage, *Energy Environ. Sci.*, 2013, **6**, 2338.

18 J. Ma, Z. Wei, L. Wang, M. Zhuo, W. Ni and H. Wang, Layered Tin Sulfide and Selenide Anode Materials for Li- and Na-ion Batteries, *J. Mater. Chem. A*, 2018, DOI: 10.1039/C8TA02695E.

19 Y. Jiang, G. Zou, H. Hou, J. Li, C. Liu, X. Qiu and X. Ji, Composition Engineering Boosts Voltage Windows for Advanced Sodium-Ion Batteries, *ACS Nano*, 2019, **13**, 10787, DOI: 10.1021/acsnano.9b05614.

20 Y. Zhang, C. Liu, Xu Gao, Z. Luo, J. Hu, G. Zou, H. Hou, Z. Xu and X. Ji, Revealing the activation effects of high valence cobalt in $CoMoO_4$ towards highly reversible conversion, *NanoEnergy*, 2020, **68**, 104333, DOI: 10.1016/j.nanoen.2019.104333.

21 W. Guo, W. Sun and Y. Wang, Multi-Layer CuO@NiO Hollow Spheres: Microwave-Assisted Metal-Organic-Framework Derivation and Highly Reversible Structure-Matched Stepwise Lithium Storage, *ACS Nano*, 2015, **9**, 11462.

22 D. Yin, G. Huang, Z. Na, X. Wang, Q. Li and L. Wang, CuO Nanorod Arrays Formed Directly on Cu Foil from MOFs as Superior Binder-Free Anode Material for Lithium-Ion Batteries, *ACS Energy Lett.*, 2017, **2**, 1564.

23 F. Klein, R. Pinedo, B. B. Berkes, J. Janek and P. Adelhelm, Kinetics and Degradation Process of CuO as Conversion Electrode for Sodium-Ion Batteries: An Electrochemical study combined with Pressure Monitoring and DEMS, *J. Phys. Chem. C*, 2017, **121**, 8679.

24 L. Zhang, Y. Wang, D. Xie, Y. Tang, C. Wu, L. Cui, Y. Li, X. Ning and Z. Shan, *In situ* transmission electron microscopy study of the electrochemical sodiation process for a single CuO nanowire electrode, *RSC Adv.*, 2016, **6**, 11441.

25 F. Klein, R. Pinedo, P. Hering, A. Polity, J. Janek and P. Adelhelm, Reaction Mechanism and Surface Film Formation of Conversion Materials for Lithium- and Sodium-Ion Batteries: A XPS Case Study on Sputtered Copper Oxide (CuO) Thin Film Model Electrodes, *J. Phys. Chem. C*, 2016, **120**, 1400.

26 P. C. Rath, J. Patra, D. Saikia, M. Mishra, J. Chang and H. Kao, Highly enhanced electrochemical performance of ultrafine CuO nanoparticles confined in ordered mesoporous carbons as anode materials for sodium-ion batteries, *J. Mater. Chem. A*, 2016, **4**, 14222.

27 D. Li, D. Yan, X. Zhang, J. Li, T. Lu and L. Pan, Porous CuO/reduced graphene oxide composites synthesized from metal–organic frameworks as anodes for high-performance sodium-ion batteries, *J. Colloid Interface Sci.*, 2017, **497**, 350.

28 L. Wang, K. Zhang, Z. Hu, W. Duan, F. Cheng and J. Chen, Porous CuO nanowires as the anode of rechargeable Na-ion batteries, *Nano Res.*, 2014, **7**, 199.

29 Y. Liu, Y. Qiao, W. X. Zhang, P. Hu, C. J. Chen, Z. Li, L. X. Yuan, X. L. Hu and Y. H. Huang, Facile fabrication of CuO nanosheets on Cu substrate as anode materials for electrochemical energy storage, *J. Alloys Compd.*, 2014, **586**, 208.

30 S. Yuan, X. L. Huang, D. L. Ma, H. G. Wang, F. Z. Meng and X. B. Zhang, Engraving Copper Foil Give Large-Scale Binder-Free Porous CuO Arrays for a High-Performance Sodium-Ion Battery Anode, *Adv. Mater.*, 2014, **26**, 2273.

31 A. Kim, M. K. Kim, K. Cho, J. Woo, Y. Lee, S. Han, D. Byun, W. Choi and J. K. Lee, One-Step Catalytic Synthesis of CuO/CuO in Graphitized Porous Carbon Matrix Derived from the Cu-based Metal–Organic Framework for Li- and Na-Ion Batteries, *ACS Appl. Mater. Interfaces*, 2016, **8**, 19514.

32 X. Wang, Y. Liu, Y. Wang and L. Jiao, CuO Quantum Dots Embedded in Carbon Nanofibers as Binder-Free Anode for Sodium Ion Batteries with Enhanced Properties, *Small*, 2016, **12**, 4865.

33 S. Cho, Y.-k. Ahn, Z. Yin, D.-J. You, H. Kim, Y. Piao, J. Yoo and Y. S. Kim, Novel synthesis of Copper oxide/graphite composite for high performance rechargeable battery anode, DOI: 10.1002/chem.201701931.

34 J. Yang, M. Winter and J. O. Besenhard, Small particle size multiphase Li-alloy anodes for lithium-ion-batteries, *Solid State Ionics*, 1996, **90**, 281.

35 R. A. Huggins and B. A. Boukamp, *US Pat.*, 4436796, 1984.

36 P. Roy and S. K. Srivastava, Nanostructured anode materials for lithium ion batteries, *J. Mater. Chem. A*, 2015, **3**, 2454.

37 M. V. Reddy, G. V. Subba Rao and B. V. R. Chowdari, Metal Oxides and Oxysalts as Anode Materials for Li Ion Batteries, *Chem. Rev.*, 2013, **113**, 5364.

38 B. N. Ganguly, V. Verma, D. Chatterjee, B. Satpati, S. Debnath and P. Saha, Study of Gallium Oxide Nanoparticles Conjugated with β-cyclodextrin – An Application to Combat Cancer, *ACS Appl. Mater. Interfaces*, 2016, **8**, 17127.

39 L. Zhao, H. Chen, Y. Wang, H. Che, P. Gunawan, Z. Zhong, H. Li and F. Su, Facile Solvothermal Synthesis of Phase-Pure Cu_4O_3 Microspheres and Their Lithium Storage Properties, *Chem. Mater.*, 2012, **24**, 1136.

40 A. Khorsand Zak, W. H. A. Majid, M. E. Abrishami and R. Yousefi, X-ray analysis of ZnO nanoparticles by Williamson–Hall and size–strain plot methods, *Solid State Sci.*, 2011, **13**, 251.

41 K. D. Rogers and P. Daniels, An X-ray Diffraction study of the effects of heat treatment on bone mineral microstructure, *Biomaterials*, 2002, **23**, 2577.

42 Y. T. Prabhu, K. V. Rao, V. S. S. Kumar and B. S. Kumari, X-Ray Analysis by Williamson–Hall and Size–Strain Plot Methods of ZnO Nanoparticles with Fuel Variation, *World J. Nano Sci. Eng.*, 2014, **4**, 21.

43 C. Suranarayana and M. G. Norton, *X-Ray Diffraction: A Practical Approach*, Springer, New York, 1998.

44 R. Srinivasan, N. Rajeswari Yogamalar, R. Justin Joseyphus and A. Chandra Bose, Estimation of Lattice Strain, Stress, Energy Density and Crystallite size of the Spherical Yttrium Oxide Nanoparticles, *Funct. Mater. Lett.*, 2009, **2**, 131.

45 N. N. Aung and W. Zhou, Effect of grain size and twins on corrosion behaviour of AZ31B magnesium alloy, *Corros. Sci.*, 2010, **52**, 589.

46 J. Liao, M. Hotta and N. Yamamoto, Corrosion behavior of fine-grained AZ31B magnesium alloy, *Corros. Sci.*, 2012, **61**, 208.

47 Y. Domi, H. Usui, K. Sugimoto and H. Sakaguchi, Effect of Silicon Crystallite Size on its Electrochemical Performance for Lithium-Ion Batteries, *Energy Technol.*, 2019, DOI: 10.1002/ente.201800946.

48 M. Thommes, K. Kaneko, A. V. Neimark, J. P. Olivier, F. Rodriguez-Reinoso, J. Rouquerol and K. S. W. Sing, Physisorption of gases, with special reference to the evaluation of surface area and pore size distribution (IUPAC Technical Report), *Pure Appl. Chem.*, 2015, **87**, 1051.

49 K. S. W. Sing, D. H. Everett, R. A. W. Haul, L. Moscou, R. A. Pieroti, J. Rouquerol and T. Siemieniewska, Reporting Physisorption data for Gas/Solid Systems with Special Reference to the Determination of Surface Area and Porosity, *Pure Appl. Chem.*, 1985, **57**, 603.

50 M. Orita, H. Ohta and M. Hirano, Deep-ultraviolet transparent conductive β-Ga_2O_3 thin films, *Appl. Phys. Lett.*, 2000, **77**, 4166.

51 A. M. Zardkhoshoui and S. S. H. Davarani, Designing a flexible all-solid-state supercapacitor based on $CuGa_2O_4$ and FeP–rGO electrodes, *J. Alloys Compd.*, 2019, **773**, 527.

52 A. A. Ensafi, S. E. Moosavifard, B. Rezaei and S. Kamari Kaverlavani, Engineering onion-like nanoporous $CuCo_2O_4$ hollow spheres derived from bimetal–organic frameworks for high-performance asymmetric supercapacitors, *J. Mater. Chem. A*, 2018, **6**, 10497.

53 S. Kamari Kaverlavani, S. E. Moosavifard and A. Bakouei, Self-templated synthesis of uniform nanoporous $CuCo_2O_4$ double-shelled hollow microspheres for high-performance asymmetric supercapacitors, *Chem. Commun.*, 2017, **53**, 1052.

54 H. Wei, Z. Chen, Z. Wu, W. Cui, Y. Huang and W. Tang, Epitaxial growth and characterization of $CuGa_2O_4$ films by laser molecular beam epitaxy, *AIP Adv.*, 2017, **7**, 115216.

55 D. Liu, X. Mo, K. Li, Y. Liu, J. Wang and T. Yang, The performance of spinel bulk-like oxygen-deficient $CoGa_2O_4$ as an air-cathode catalyst in microbial fuel cell, *J. Power Sources*, 2017, **359**, 355.

56 X. Yu, X. An, A. Shavel, M. Ibanez and A. Cabot, The effect of the Ga content on the photocatalytic hydrogen evolution of $CuIn_{1-x}Ga_xS_2$ nanocrystals, *J. Mater. Chem. A*, 2014, **2**, 12317.

57 C. Ye, M. D. Regulacio, S. H. Lim, Q. H. Xu and M. Y. Han, Colloidal Nanocrystals of Wurtzite-Type Cu_2ZnSnS_4: Facile Noninjection Synthesis and Formation Mechanism, *Chem.–Eur. J.*, 2012, **18**, 11258.

58 *NIST-XPS database*, version 3.5, http://srdata.nist.gov/xps/.

59 H. Yan, Y. Lu, K. Zhu, T. Peng, X. Liu, Y. Liu and Y. Luo, Growth of highly mesoporous $CuCo_2O_4$@C core–shell arrays as advanced electrodes for high-performance supercapacitors, *Appl. Surf. Sci.*, 2018, **439**, 883.

60 W. Song, J. Lischner, V. G. Rocha, H. Qin, J. Qi, H. L. Joseph, *et al.*, Tuning the Double Layer of Graphene Oxide through Phosphorus Doping for Enhanced Supercapacitance, *ACS Energy Lett.*, 2017, **2**, 1144–1149, DOI: 10.1021/acsenergylett.7b00275.

61 N. M. Vuong, *et al.*, CuO-Decorated ZnO Hierarchical Nanostructures as Efficient and Established Sensing Materials for H_2S Gas Sensors, *Sci. Rep.*, 2016, **6**, 26736.

62 L. Zhao, H. Chen, Y. Wang, H. Che, P. Gunawan, Z. Zhong, H. Li and F. Su, Facile Solvothermal Synthesis of Phase-Pure Cu_4O_3 Microspheres and Their Lithium Storage Properties, *Chem. Mater.*, 2012, **24**, 1136.

63 P. C. Rath, J. Patra, D. Saikia, M. Mishra, C.-M. Tseng, J.-K. Chang and H.-M. Kao, A Comparative Study on the Morphology-Dependent Performance of Various CuO Nanostructures as Anode Materials for Sodium-Ion Batteries, *ACS Sustainable Chem. Eng.*, 2018, **6**, 10876.